Nanoscale Advances

ROYAL SOCIETY OF CHEMISTRY

PAPER

View Article Online
View Journal | View Issue

Cite this: *Nanoscale Adv.*, 2026, **8**, 2065

Tetranuclear Ag(I) and Au(I) nano-sized $[L_2(R)_8 \rightarrow M_4]^{4+}$ (M = Ag(I) and Au(I); R = C_2H_5, CH_3, H, F, Cl, Br, Ph and SiH_3) complexes: nature and cooperativity of metal–ligand bonds

Sepideh Goodarzi,[a] Mehdi Bayat, *[b] Sadegh Salehzadeh [a] and Ehsan Alavipour[a]

Received 10th September 2025
Accepted 7th February 2026

DOI: 10.1039/d5na00870k

rsc.li/nanoscale-advances

NHC ligands are able to stabilize different metals in different oxidation states and coordination geometries, making them interesting candidates for the synthesis of potent metal-based anti-cancer agents. This study explores the bonding characteristics and nature of cooperativity in tetranuclear cationic complexes of Ag(I) and Au(I), formulated as $[L_2(R)_8 \rightarrow M_4]^{4+}$ (M = Ag(I) and Au(I); R = C_2H_5, CH_3, H, F, Cl, Br, Ph and SiH_3), with potential antibacterial and anticancer properties using DFT calculations at the PBE-D3-B3LYP/def2-SVP//PBE-D3/def2-TZVP level. Bond cooperativity, evaluated through interaction energies, and the resulting data indicated that there is an anti-cooperativity behavior among the metal–ligand interactions. EDA results confirm that electrostatic contributions are found to be dominant, suggesting that the $C_{NHC} \rightarrow M$ bonds in these complexes are primarily electrostatic in nature.

Introduction

N-Heterocyclic carbenes (NHCs) are a class of ligands where the carbene center is incorporated within a nitrogen-containing heterocycle, which contributes to both their reactivity and initial challenges in isolation.[1] Today, many NHCs are commercially available, and their chemistry has become foundational in organometallic research, often rivaling the performance of traditional tertiary phosphines.[1–4] Due to their strong σ-donating ability, NHCs tend to form more robust metal–ligand bonds than phosphines.[3] Over the past three decades, the utilization of NHCs as ligands has expanded significantly, largely owing to the synthetic accessibility and high stability of metal–NHC complexes.[4–10] Within coordination chemistry, NHC ligands have shown exceptional promise, particularly with group 11 metals such as silver(I) and gold(I). Multinuclear Ag(I) and Au(I) complexes supported by NHC ligands exhibit distinct structural and electronic features, which underpin their catalytic activity and potential applications in molecular recognition and materials science.[11,12] These NHC–metal complexes have attracted increasing attention for their biomedical relevance, especially as potential antimicrobial and anticancer agents,[13–15] in addition to their established roles in catalysis.[16,17] Silver–NHC complexes, in both mono- and multinuclear forms, have been widely explored for their unique physicochemical properties and multifunctional applications across chemistry, medicine, and materials science.[18–23] They exhibit notable antibacterial and cytotoxic activities, positioning them among the leading candidates in pharmaceutical research.[24,25] Similarly, Au(I)–NHC complexes have emerged as potent alternatives to phosphine-based gold complexes (*e.g.*, R_3P–Au(I)) in anticancer drug development.[26] Their high air stability, strong Au–C bonds,

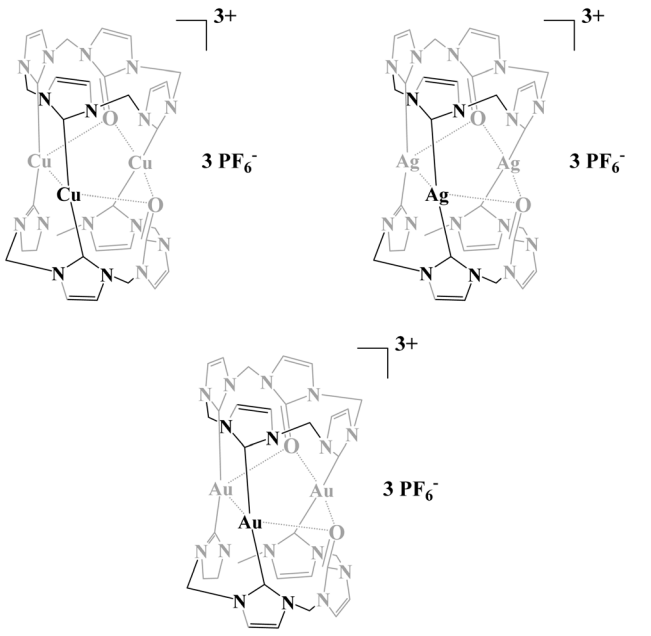

Fig. 1 The structure of the pharmaceutical complexes studied by Jacob.[36]

[a]*Department of Inorganic Chemistry, Faculty of Chemistry and Petroleum Sciences, Bu-Ali Sina University, Hamedan, Iran*

[b]*School of Chemistry, College of Science, University of Tehran, Tehran, Iran. E-mail: bayatm@ut.ac.ir; mehdi806@gmail.com*

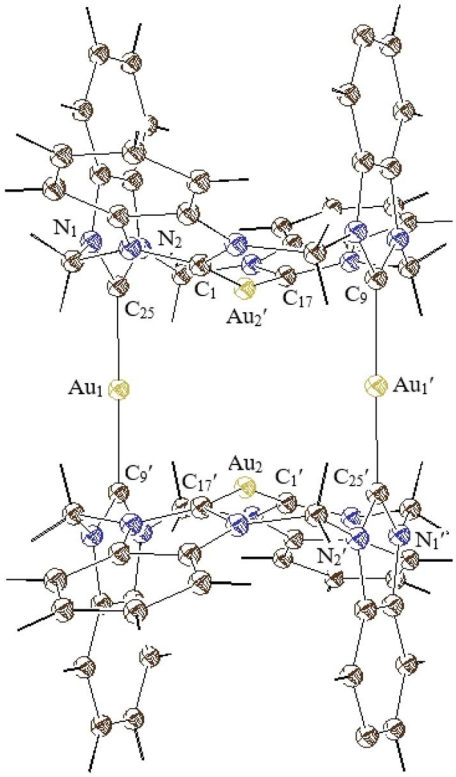

Fig. 2 The solid-state molecular structure of a tetra-nuclear gold cluster synthesized by Jacob.[43]

and synthetic tunability make them particularly attractive for designing metal-based therapeutic agents.[27–35] Notably, Jacob and co-workers synthesized and characterized large cyclic trinuclear tricarbene complexes involving Cu(I), Ag(I), and Au(I), which were evaluated for antimicrobial efficacy against *Staphylococcus aureus* and *Escherichia coli*, as well as anticancer activity against HeLa and MCF-7 cell lines.[36] Among these, silver complexes displayed significant antiproliferative effects, with IC_{50} values ranging from 3.03 μM to 25.01 μM (ref. 36) (Fig. 1).

In recent years, substantial attention has been directed toward elucidating the structural and electronic features of metal–NHC interactions, particularly in pharmaceutically relevant Ag(I) and Au(I) complexes.[37–41]

Recently, we have reported a theoretical study on the structural and bonding characteristics of M ← C bonds in trinuclear, nanosized Cu(I), Ag(I), and Au(I) cations with two tris-NHC ligands, which exhibit promising anti-cancer and antibacterial potential. The results indicate that not only all complexes exhibit positive cooperativity values, suggesting anti-cooperativity but also the ΔE_{elstat} accounted for the largest share, indicating that the interaction between the fragments is predominantly electrostatic.[42]

Herein, a comparative theoretical investigation is presented on tetranuclear cationic clusters of Ag(I) and Au(I), formulated as $[L_2(R)_8 \rightarrow M_4]^{4+}$, where two symmetric tetra-NHC ligands (L) coordinate with four metal centers. The influence of various substituents (R = C_2H_5, CH_3, H, F, Cl, Br, SiH_3 and Ph) on the NHC rings was systematically evaluated to assess their effect on bonding characteristics within these clusters. Notably, the

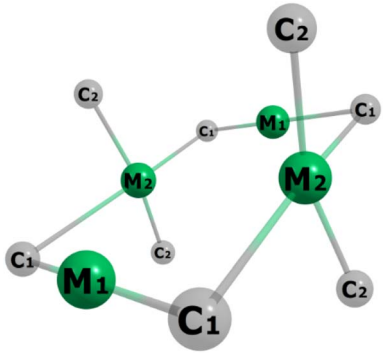

Fig. 3 Selected atom numbering in the structure of $[L_2(R)_8 \rightarrow M_4]^{4+}$ complexes, M = Au(I) and Ag(I).

crystallographic data of a phenyl-substituted tetranuclear gold complex, synthesized and structurally characterized by Bauer *et al.* in 2019,[43] were used as the initial geometry input for the computational analysis conducted in this study (Fig. 2).

Computational details

Based on Fig. 3, there are three types of M–$C_{(NHC)}$ bonds in the corresponding complex, as illustrated in Fig. 3. The optimized structure of this complex was calculated using eight different DFT methods (See Table 1). The deviations of the corresponding bond lengths were then computed for each method, and the root-mean-square deviation (RMSD) values were determined to quantitatively assess how well each method reproduces the experimental reference data. Among the tested functionals, the PBE-D3 method demonstrated the closest agreement with the experimental metrics, as indicated by the lowest RMSD values. These results identify PBE-D3 as the most reliable method for further analysis in this study. To evaluate the accuracy of each functional, root-mean-square (RMS) deviations between computed and experimental bond parameters were calculated. Among the tested functionals, the PBE-D3 method demonstrated the closest agreement with experimental metrics, as indicated by the lowest RMS error values. These results, summarized in Table 1, identify PBE-D3 as the most reliable method for further analysis in this study.[44,45]

The geometry of the investigated complexes was fully optimized in the gas phase at the PBE-D3/def2-SVP level of theory using the Gaussian 09 software package.[46] Single-point energy

Table 1 RMSD calculation of $[L_2(Ph)_8 \rightarrow Au_4]^{4+}$ complexes (all values are given in Å)

Method	Au_1–$C_{(NHC)1}$	$C_{(NHC)1}$–Au_2	Au_1–$C_{(NHC)1}$	RMSD
M05-D3	2.10	2.80	2.10	0.09
BLYP-D3	2.08	2.86	2.09	0.10
BP86-D3	2.06	2.82	2.07	0.07
CAM-B3LYP-D3	2.07	2.80	2.07	0.07
M05-2X-D3	2.07	2.78	2.08	0.07
M06-D3	2.09	2.82	2.11	0.10
M06-2X-D3	2.08	2.82	2.09	0.09
PBE-D3	**2.06**	**2.76**	**2.07**	**0.05**
Experimental data	2.02	2.68	2.03	—

calculations and Natural Bond Orbital (NBO) analyses were subsequently performed at the PBE-D3/def2-TZVP//PBE-D3/def2-SVP level of theory. Harmonic vibrational frequency calculations were carried out to verify that the optimized structures correspond to local minima on the potential energy surface, as confirmed by the absence of imaginary frequencies. To explore the nature of chemical bonds between the tetrakis-NHC ligand framework and the metal ion in the M_4^{4+} fragment ($C_{4NHC} \rightarrow M_4$), NBO analysis was conducted at the PBE-D3/def2-TZVP//PBE-D3/def2-SVP level of theory. Additionally, Energy Decomposition Analysis combined with Natural Orbitals for Chemical Valence (EDA-NOCV) was employed to dissect the bonding interactions within the complexes. These calculations were carried out at the BP86-D3/TZ2P//PBE-D3/def2-SVP level of theory using the ADF 2013 software suite.[47]

Results and discussion

Structural aspects

The optimized geometries of the $[L_2(R)_8 \rightarrow M_4]^{4+}$ complexes (M = Ag(I), Au(I)); (R = C_2H_5, CH_3, H, F, Cl, Br, SiH_3 and Ph) and their selected bond lengths and atom–atom distances are illustrated in Fig. 4–6. All geometrical optimizations were conducted in the gas phase using the PBE-D3/def2-SVP level of theory. To evaluate solvent effects, the $[L_2(Ph)_8 \rightarrow Au_4]^{4+}$ and $[L_2(Ph)_8 \rightarrow Ag_4]^{4+}$ complexes were selected as representative systems. Single-point calculations were performed at the PBE-D3/def2-SVP level of theory using implicit solvation models with acetonitrile as the solvent. For the $[L_2(Ph)_8 \rightarrow Au_4]^{4+}$ complex, three continuum solvation models (SMD, CPCM, and IEFPCM) were applied, whereas for the $[L_2(Ph)_8 \rightarrow Ag_4]^{4+}$ complex only the SMD model was employed, followed by interaction energy evaluation (results are collected in Table S2). The results indicate that the computed interaction energies in solution are substantially larger than those obtained in the gas phase, suggesting an overestimation of stabilization effects by the implicit solvent models. Therefore, gas-phase calculations are considered more appropriate and reliable for describing the fundamental bonding characteristics of the complexes investigated in this study.

To assess the bonding environment across the entire $[L_2(R)_8 \rightarrow M_4]^{4+}$ series, where M = Au(I) and Ag(I); (R = C_2H_5, CH_3, H, F, Cl, Br, SiH_3 and Ph), the minimum and maximum $C_{(NHC)} \rightarrow M$ bond distances were evaluated. As shown in Fig. 3, three distinct metal–carbon bonding motifs were identified: C_1–M_1, C_1–M_2, and C_2–M_2. In the silver complexes, these bond lengths ranged from 2.09 to 2.11 Å (C_1–M_1), 2.67 to 2.70 Å (C_1–M_2), and 2.10 to 2.14 Å (C_2–M_2). The corresponding values for the gold complexes are 2.05 to 2.06 Å, 2.73 to 2.76 Å, and 2.05 to 2.07 Å, respectively. Notably, changes in the R substituents on the NHC rings had minimal impact on the overall M–C bond distances, suggesting a high degree of structural robustness across the series. A comprehensive list of all $C_{(NHC)} \rightarrow M$ bond lengths in the mentioned complexes is provided in the SI (Table S1).

To measure the approximate size of complexes, $[L_2(R)_8 \rightarrow M_4]^{4+}$ series (R = C_2H_5, CH_3, H, F, Cl, Br, SiH_3 and Ph), the distance between H, F, Cl, Br, C or Si atoms of R groups of two coordinated ligands was calculated. These distances are indicated by red lines in the optimized geometries (See Fig. 4–6). Structural data confirmed that this series of complexes exhibits a nanoscale structure (See Fig. 4–6).

Interaction energies

The interaction energies (ΔE_{int}) between the M_4^{4+} metal cluster and two $L(R)_4$ ligands within the optimized structure of the complexes are computed at the PBE-D3/def2-TZVP//PBE-D3/def2-SVP level of theory (See Table 2). To systematically evaluate the interaction energies in the $[L_2(R)_8 \rightarrow M_4]^{4+}$ complexes, the system is partitioned into three fragments A, A′, and B illustrated in Fig. 7. As can be seen, the central M_4^{4+} metal cluster is considered as fragment B and two coordinated $L(R)_4$ ligands as fragments A and A′. Each ABA′ complex was considered as a three-component ABC system and the total interaction energy can be calculated *via* the common eqn (1) and also eqn (2) (ref. 48) and (3) (ref. 49) that all give the same value.

$$IE_{total} = E_{ABC} - (E_{A^{ABC}} + E_{B^{ABC}} + E_{C^{ABC}}) \quad (1)$$

$$IE_{total} = \frac{1}{2}\left(IE^{ABC}_{A-B} + IE^{ABC}_{B-C} + IE^{ABC}_{A-BC} + IE^{ABC}_{AB-C}\right) \quad (2)$$

$$IE_{total} = IE^{ABC}_{A-BC} + IE^{ABC}_{B-C} = IE^{ABC}_{AB-C} + IE^{ABC}_{A-B} \quad (3)$$

In the above equations, E_{ABC} is the energy of the optimized geometry of the ABC system, and E_A^{ABC}, E_B^{ABC} and E_C^{ABC} are the energies of A, B and C fragments, respectively, frozen in the optimized geometry of the ABC system. On the other hand, IE^{ABC}_{A-B}, IE^{ABC}_{B-C}, IE^{ABC}_{A-BC} and IE^{ABC}_{AB-C} correspond to the A–B, B–C, A–BC and AB–C interaction energies in the optimized geometry of the ABC system. In the present complexes where the A and C are the same ligands we can name the ABC system as ABA′, and the related IE^{ABC}_{A-B}, IE^{ABC}_{B-C}, IE^{ABC}_{A-BC} and IE^{ABC}_{AB-C} terms as $IE^{ABA'}_{A-B}$, $IE^{ABA'}_{B-A'}$, $IE^{ABA'}_{A-BA'}$ and $IE^{ABA'}_{AB-A'}$, respectively. Interaction energies for the corresponding complexes were computed using all three formulas, and the results demonstrated complete consistency among the methods.

The calculated total interaction energies for Ag(I) and Au(I) within the $[L_2(R)_8 \rightarrow M_4]^{4+}$ complexes range from −830.25 to −979.63 kcal mol^{-1} for silver and from −1016.53 to −1171.62 kcal mol^{-1} for gold complexes. Maintaining a constant R substituent, the gold-based complexes consistently demonstrated stronger interaction energies than their silver analogues. For instance, the total interaction energies for $[L_2(C_2H_5)_8 \rightarrow Au_4]^{4+}$ and $[L_2(C_2H_5)_8 \rightarrow Ag_4]^{4+}$ were determined to be −1171.62 and 979.63 kcal mol^{-1}, respectively. Complexes with the Ph group as the R substituent and electron-donating groups such as C_2H_5 and CH_3 exhibited elevated interaction energies compared to those bearing electron-withdrawing R groups like F, Br, and Cl. This trend was consistent across both silver and gold clusters. The most pronounced interaction energy was observed in $[L_2(C_2H_5)_8 \rightarrow Au_4]^{4+}$ (−1171.62 kcal mol^{-1}), while the lowest was found in $[L_2(F)_8 \rightarrow Ag_4]^{4+}$ (−830.25 kcal mol^{-1}).

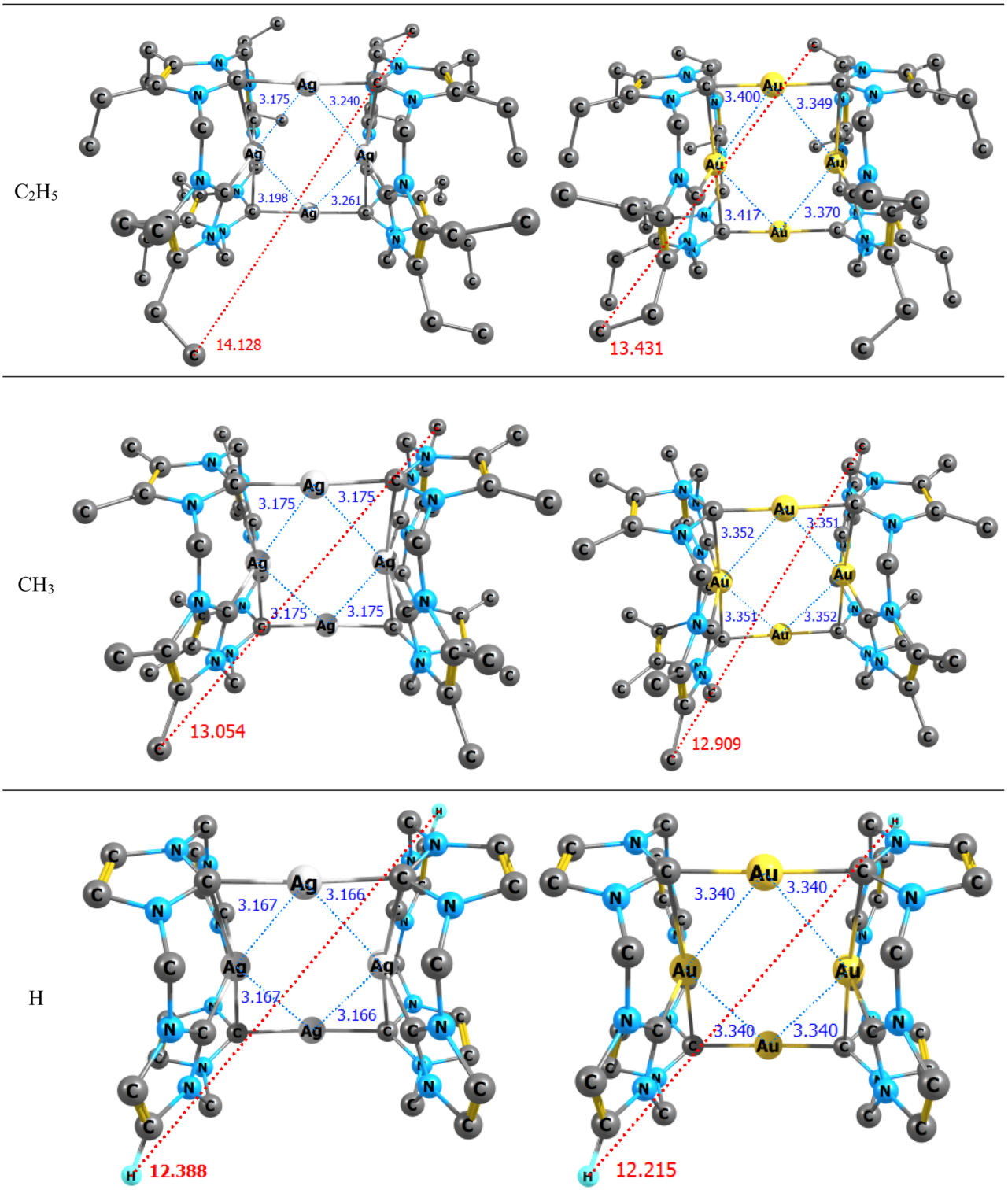

Fig. 4 The optimized structures and selected bond lengths and atom–atom distances of $[L_2(R)_8 \rightarrow M_4]^{4+}$ complexes; M = Ag(I) and Au(I); R = C_2H_5, CH_3 and H.

Cooperativity

Cooperativity describes situations in which the formation of one bond influences the strength of subsequent bonding events, leading to nonadditive interaction energies. This phenomenon is widely recognized in biological systems and supramolecular chemistry, where it plays a central role in regulating complex molecular assemblies and multivalent interactions.[50–52] Early theoretical studies conceptualized cooperativity using triads and pairwise nonadditivity models;[53–60]

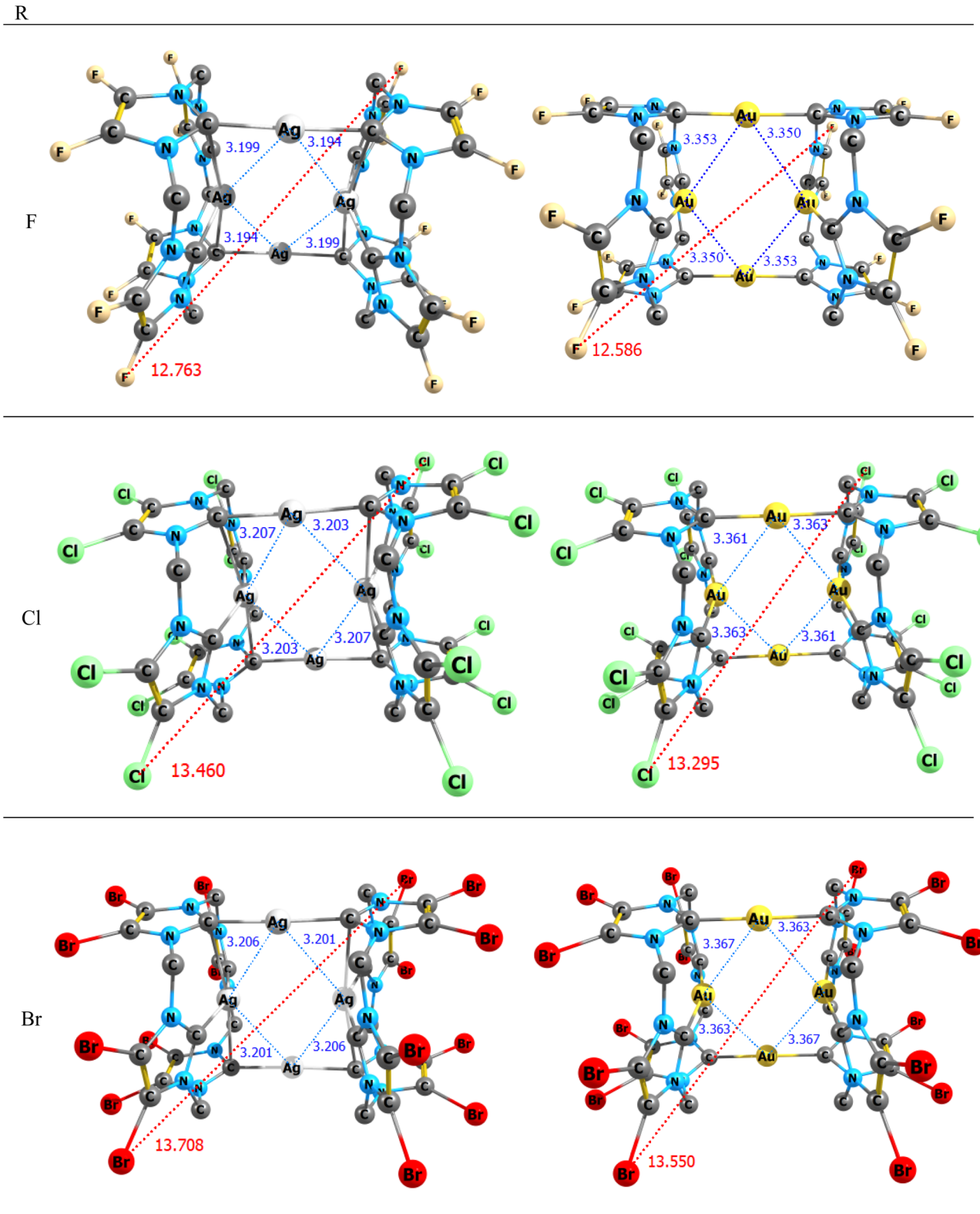

Fig. 5 The optimized structures and selected bond lengths and atom–atom distances of $[L_2(R)_8 \rightarrow M_4]^{4+}$ complexes; M = Ag(I) and Au(I); R = F, Cl and Br.

additional methodological details and derivations of these models are provided in the SI. More recent studies have extended these approaches to quantify cooperativity in compounds with covalent bonds, including metal–ligand interactions.[49,61,62]

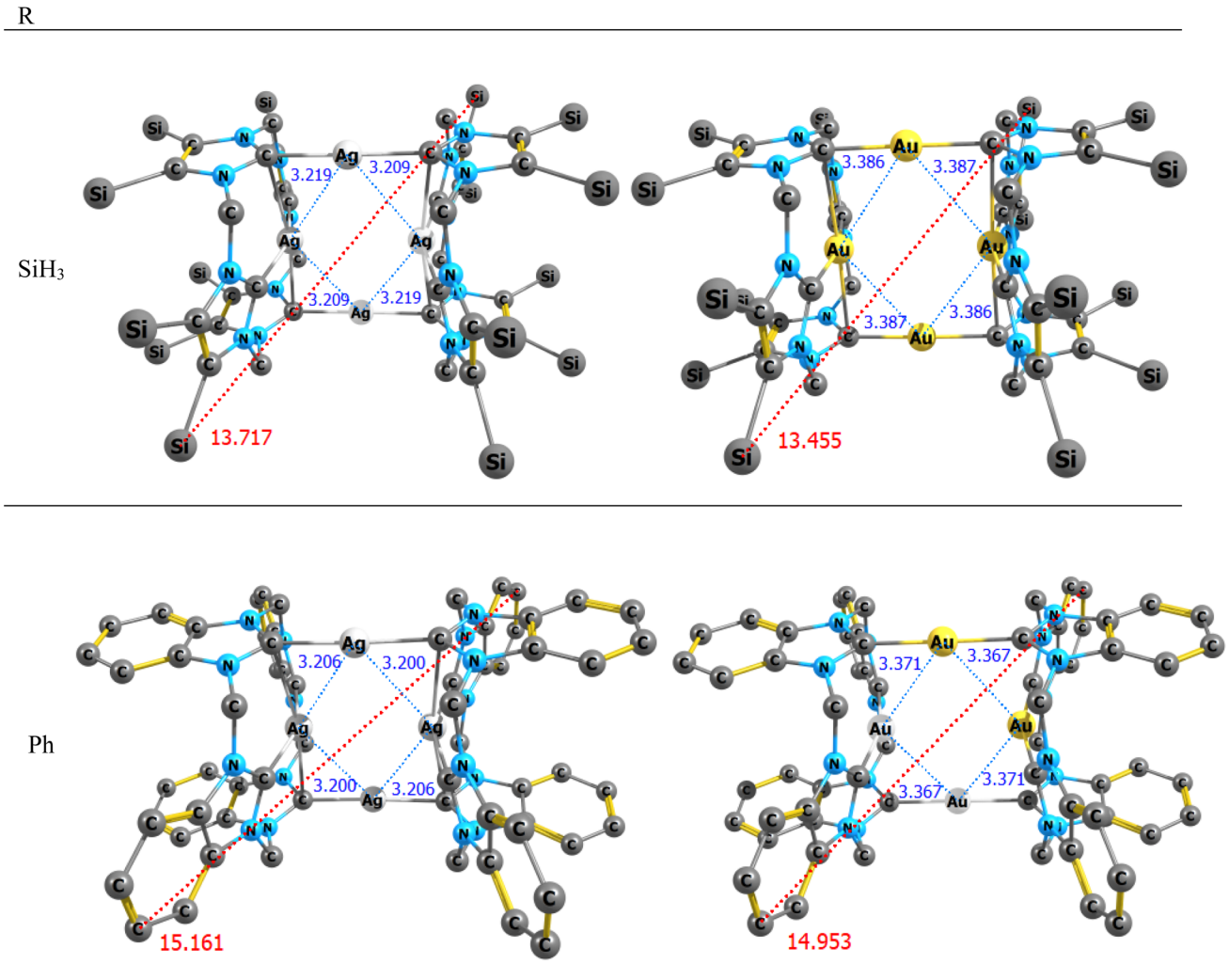

Fig. 6 The optimized structures and selected bond lengths and atom–atom distances of $[L_2(R)_8 \rightarrow M_4]^{4+}$ complexes; M = Ag(I) and Au(I); R = SiH_3 and Ph.

In multinuclear metal complexes, cooperativity arises from electronic communication, electrostatic effects, and orbital saturation within confined metal cores. In the present study, cooperativity was quantified using an interaction-energy-based approach that evaluates the incremental change in metal–ligand interaction strength upon successive bond formation.[49,61] A positive cooperativity energy ($\Delta\Delta E_{int}$) corresponds to anti-cooperative behavior, indicating that the formation of additional metal–ligand bonds weakens subsequent interactions due to electronic saturation and electrostatic repulsion effects. Detailed derivations, mathematical expressions, and example calculations are provided in the SI (See Section S1).

The calculated cooperativity energies for the tetranuclear $[L_2(R)_8 \rightarrow M_4]^{4+}$ complexes (M = Ag(I), Au(I)) are summarized in Table 2. All investigated systems exhibit positive cooperativity values, confirming their anti-cooperative nature. Consistent with the interaction energy trends, Au(I) complexes systematically display larger anti-cooperativity energies than their Ag(I) counterparts. For instance, the cooperativity energies for $[L_2(F)_8 \rightarrow Ag_4]^{4+}$ and $[L_2(F)_8 \rightarrow Au_4]^{4+}$ are 175.85 and 229.49 kcal mol^{-1}, respectively. Anti-cooperative behavior is observed across all tetranuclear clusters, with electron-donating substituents generally promoting slightly stronger anti-cooperative effects compared to electron-withdrawing groups. The observed positive (anti-cooperative) behavior in the tetranuclear NHC-stabilized clusters indicates an uneven distribution of bonding strength among metal–ligand interactions. Although direct reactivity studies were not performed, this cooperativity provides conceptual insight into differential stability, which could be relevant to the function of analogous multinuclear supramolecular assemblies.

Comparison with previously reported trinuclear Cu(I), Ag(I), and Au(I) complexes shows that although anti-cooperative behavior is already present in lower-nuclearity systems, the magnitude of anti-cooperativity is significantly enhanced in the tetranuclear assemblies investigated here.[42] This enhancement reflects increased electronic crowding, electrostatic repulsion, and intermetallic communication within higher-nuclearity metal cores.

Table 2 The values of A–B, B–A′, A–BA′ and AB–A′ interaction energies, total interaction energies and cooperativity of bonds (kcal mol^{-1}) in $[L_2(R)_8 \rightarrow M_4]^{4+}$ complexes; M = Ag(I) and Au(I); R = C_2H_5, CH_3, H, F, Cl, Br, SiH_3 and Ph

M	R	$IE^{ABA'}_{A-B}$	$IE^{ABA'}_{B-A'}$	$IE^{ABA'}_{A-BA'}$	$IE^{ABA'}_{AB-A'}$	$IE_{total\ (eqn\ (1)-(3))}$	ΔIE_{coop}
Ag	C_2H_5	−613.65	−612.72	−366.91	−365.98	−979.63	246.74
	CH_3	−601.61	−601.61	−367.83	−367.83	−969.44	233.78
	H	−546.21	−546.38	−360.48	−360.64	−906.86	185.73
	F	−503.13	−503.13	−327.12	−327.12	−830.25	176.01
	Cl	−531.93	−531.93	−323.95	−323.95	−855.88	207.98
	Br	−546.77	−546.77	−321.04	−321.04	−867.81	225.73
	SiH_3	−577.79	−577.79	−352.47	−352.47	−930.26	225.32
	Ph	−580.31	−580.31	−347.18	−347.18	−927.49	233.13
Au	C_2H_5	−739.53	−741.23	−430.39	−432.1	−1171.62	309.14
	CH_3	−725.6	−725.6	−430.52	−430.52	−1156.13	295.08
	H	−664.74	−664.74	−428.13	−428.13	−1092.87	236.61
	F	−619.54	−619.54	−396.98	−396.98	−1016.53	222.56
	Cl	−682.99	−682.99	−397.77	−397.77	−1080.76	285.22
	Br	−667.05	−667.26	−387.75	−387.96	−1055.01	279.3
	SiH_3	−702.25	−702.25	−418.73	−418.73	−1120.98	283.52
	Ph	−702.35	−702.35	−414.70	−414.70	−1117.05	287.65

NBO analysis

NBO (Natural Bond Orbital) analysis is a powerful tool for studying metal–ligand interactions, offering detailed insights into bonding, charge transfer, and coordination characteristics.[63] In this study, Gaussian 09 software was employed for NBO analysis. Using NBO calculations at the PBE-D3/def2-TZVP level of theory, the nature of the $C_{(tetrakis\text{-}NHC)} \rightarrow M_4$ bonds in the specified complexes was examined.

Natural charges on the M_4^{4+} fragment within the $[L_2(R)_8 \rightarrow M_4]^{4+}$ complexes (where M = Ag(I) or Au(I), and R = C_2H_5, CH_3, H, F, Cl, Br, SiH_3 and Ph) were calculated using the PBE-D3/def2-TZVP method (See Table 3). In these complexes, the formal charges on the M_4 and $L_2(R)_8$ fragments are +4 and 0, respectively. The data indicate charge transfer from the $L_2(R)_8$ ligand fragments to the M_4^{4+} metal ion cluster in mentioned complexes. For a fixed substituent R, the natural charge on the M_4^{4+} fragment decreases when moving from Ag(I) to Au(I). For example, the natural charges for the M_4^{4+} fragment in $[L_2(Ph)_8 \rightarrow Ag_4]^{4+}$ and $[L_2(Ph)_8 \rightarrow Au_4]^{4+}$ are 1.38*e* and 0.91*e*, respectively. Variation in the R substituent produces only minor changes; for instance, the charges on M_4^{4+} fragments in $[L_2(F)_8 \rightarrow Ag_4]^{4+}$ and $[L_2(C_2H_5)_8 \rightarrow Ag_4]^{4+}$ are 1.35*e* and 1.39*e*, respectively. The highest and lowest values of natural charges are observed in $[L_2(Cl)_8 \rightarrow Ag_4]^{4+}$ (1.52*e*) and $[L_2(C_2H_5)_8 \rightarrow Au_4]^{4+}$ (0.82*e*), respectively. Furthermore, the degree of charge transfers from $L_2(R)_8$ to M_4^{4+} fragments increases when the metal changes from Ag(I) to Au(I) for the same substituent. For example, charge transfer values in $[L_2(Br)_8 \rightarrow Ag_4]^{4+}$ and $[L_2(Br)_8 \rightarrow Au_4]^{4+}$ are −2.63*e* and −3.10*e*, respectively. Changes in substituents have minimal effect on the charge transfer values; for instance, the values of −3.18*e* and −3.14*e* are observed for

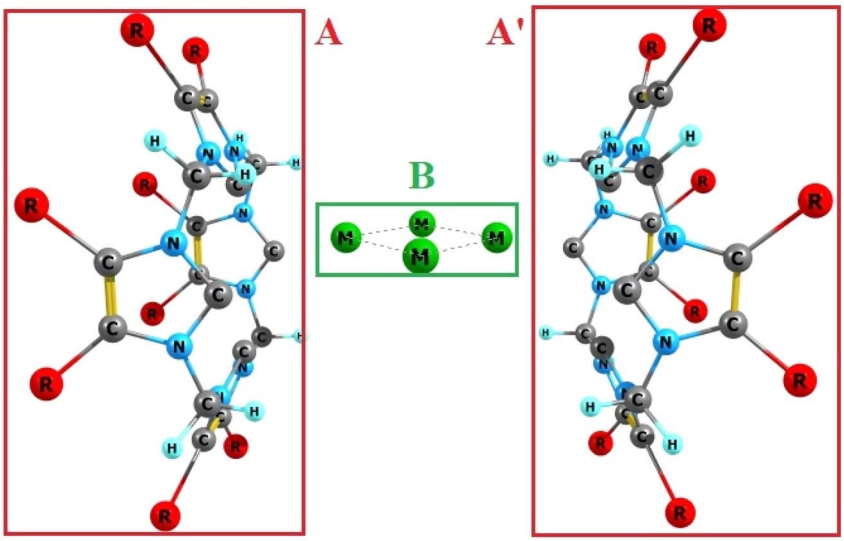

Fig. 7 Fragments of $[L_2(R)_8 \rightarrow M_4]^{4+}$ complexes; M = Ag(I) and Au(I); R = C_2H_5, CH_3, H, F, Cl, Br, SiH_3 and Ph.

Table 3 Natural charges and the amount of charge transfer between $L_2(R)_8$ and M_4^{4+} fragments in $[L_2(R)_8 \rightarrow M_4]^{4+}$ complexes; M = Ag(I) and Au(I); R = C_2H_5, CH_3, H, F, Cl, Br, SiH_3 and Ph

		Natural charge		Charge transfer (e)
M	R	M_4	$L_2(R)_8$	$L_2(R)_8 \rightarrow M_4$
Ag	C_2H_5	1.39	2.61	−2.61
	CH_3	1.37	2.63	−2.63
	H	1.39	2.61	−2.61
	F	1.35	2.65	−2.65
	Cl	1.52	2.48	−2.48
	Br	1.37	2.63	−2.63
	SiH_3	1.39	2.61	−2.61
	Ph	1.38	2.62	−2.62
Au	C_2H_5	0.82	3.18	−3.18
	CH_3	0.89	3.11	−3.11
	H	0.90	3.10	−3.10
	F	0.86	3.14	−3.14
	Cl	0.89	3.11	−3.11
	Br	0.90	3.10	−3.10
	SiH_3	0.91	3.09	−3.09
	Ph	0.91	3.09	−3.09

Table 4 Wiberg bond index of $L_2(R)_8 \rightarrow M_4$ for $[L_2(R)_8 \rightarrow M_4]^{4+}$ complexes; M = Ag(I) and Au(I); R = C_2H_5, CH_3, H, F, Cl, Br, SiH_3 and Ph

		Wiberg index		
M	R	M_1–$C_{(NHC)1}$	M_2–$C_{(NHC)2}$	M_2–$C_{(NHC)1}$
Ag	F	0.40	0.43	0.16
Ag	Cl	0.40	0.42	0.15
Ag	Br	0.39	0.37	0.18
Ag	C_2H_5	0.40	0.41	0.15
Ag	CH_3	0.42	0.43	0.16
Ag	H	0.40	0.42	0.15
Ag	SiH_3	0.40	0.40	0.14
Ag	Ph	0.41	0.41	0.14
Au	F	0.55	0.61	0.13
Au	Cl	0.55	0.60	0.13
Au	Br	0.55	0.59	0.16
Au	C_2H_5	0.55	0.60	0.13
Au	CH_3	0.55	0.60	0.14
Au	H	0.55	0.60	0.14
Au	SiH_3	0.54	0.60	0.13
Au	Ph	0.55	0.60	0.13

$[L_2(C_2H_5)_6 \rightarrow Au_3]^{3+}$ and $[L_2(F)_6 \rightarrow Au_3]^{3+}$, respectively. The results suggest ligand-to-metal charge transfer (LMCT) as the dominant interaction behavior among the metal–ligand bonds.

The chemical bond orders of the $C_{(tetrakis\text{-}NHC)} \rightarrow M_4$ in the $[L_2(R)_8 \rightarrow M_4]^{4+}$ complexes, where M = Ag(I) or Au(I) and R = C_2H_5, CH_3, H, F, Cl, Br, SiH_3 and Ph were evaluated using the Wiberg bond index (WBI) method (See Table 4). In the $[L_2(R)_8 \rightarrow M_4]^{4+}$; M = Ag(I) or Au(I) complexes, three distinct types of M–C bonds and atom numbering are identified in Fig. 3. Replacing Ag(I) with Au(I) at the M_4^{4+} center, while keeping the R groups on the ligand constant, results in higher WBI values for the M_1–$C_{(NHC)1}$ and M_2–$C_{(NHC)2}$ bonds in the gold complexes compared to their silver counterparts. However, the WBI for the M_2–$C_{(NHC)1}$ bond shows a minor reduction when the metal is substituted from silver to gold. Additionally, variations in the R substituents have little effect on the Wiberg bond indices of the complexes studied. Fig. 3 presents the same structural illustration shown in the bond length section.

Natural Hybrid Orbitals (NHOs), derived within the Natural Bond Orbital (NBO) framework, characterize the hybridization of atomic orbitals in a molecule. Table 5 summarizes the NHO analysis results for the M and C atoms involved in the $C_{(tetrakis\text{-}NHC)} \rightarrow M_4$ bonds of the $[L_2(R)_8 \rightarrow M_4]^{4+}$ complexes, where M represents Ag(I) or Au(I), and R denotes C_2H_5, CH_3, H, F, Cl, Br, SiH_3 and Ph. The carbon atom occupancy in these bonds averages around 76% for Au(I) and 84% for Ag(I) complexes with negligible variation due to changes in the R substituents.

The results are in good agreement with our previous studies[64,65] and show that the $C_{(tetrakis\text{-}NHC)} \rightarrow M_4$ bonding interaction arises from the σ donation of a lone pair on $C_{(tetrakis\text{-}NHC)}$ as a Lewis base to the empty orbitals of the M_4^{4+} fragments as a Lewis acid (Table 5). The NHO analysis reveals that the d-orbital occupancy in gold complexes is higher than in silver complexes; therefore, the ΔE_{orb} contribution in gold complexes is expected to be greater than in silver. On the other hand, an increase in carbon orbital occupancy indicates a stronger σ-donation from the NHC to the metal, which consequently enhances the covalent character of the bond and increases the ΔE_{orb} value in the EDA analysis. For this reason, the percentage of ΔE_{orb} in silver and gold complexes is found to be close.

Donor–acceptor interactions were further examined using the Fock matrix within the NBO analysis framework. Table 6 details these interactions for complexes containing both electron-donating and electron-withdrawing substituents. According to second-order perturbation theory, the σ* and lone pair (Lp*) orbitals of the metal center in the $C_{(tetrakis\text{-}NHC)} \rightarrow M_4$ bonds are populated by electron density donated from the carbon lone pairs. The most prominent donor–acceptor interactions involve electron donation from the $C_{(tetrakis\text{-}NHC)}$ lone pair to the σ* antibonding orbitals of Ag(I) and Au(I), corresponding to $C_{(tetrakis\text{-}NHC} \rightarrow Ag(I)$ and $C_{(tetrakis\text{-}NHC} \rightarrow Au(I)$ transitions. In gold complexes, the stronger σ-donation from the NHC ligand enhances the overlap between filled orbitals, thereby increasing both ΔE_{Pauli} and $E(2)$. This effect, corroborated by donor–acceptor and energy decomposition analyses, demonstrates that gold complexes experience greater Pauli repulsion and stronger donor–acceptor interactions than their silver analogues.

Energy decomposition analysis (EDA)

Energy Decomposition Analysis (EDA)[66] is a computational chemistry method used to break down the total interaction energy between two or more molecular fragments into distinct, physically meaningful components. This technique allows for a detailed understanding of how different factors contribute to the overall bonding interactions between molecules or molecular fragments. EDA combined with Natural Orbital for

Table 5 Natural hybrid orbital (NHO) analysis of $[L_2(R)_8 \rightarrow M_4]^{4+}$ complexes; M = Ag(I) and Au(I); R = C_2H_5, CH_3, H, F, Cl, Br, SiH_3 and Ph

	C_2H_5		CH_3		H		F		Cl		Br		SiH_3		Ph	
Occupancy	Ag	C	Ag	C	Ag	C	Ag	C	Ag	C	Ag	C	Ag	C	Ag	C
Occupancy Ag–C	1.84553		1.84536		1.84557		1.84851		1.84510		1.84313		1.84286		—	
%	15.93	84.07	15.90	84.10	15.66	84.34	15.49	84.51	15.54	84.46	15.57	84.43	15.82	84.18	—	—
%s	86.14	42.54	86.20	42.33	86.47	42.52	86.14	42.31	86.34	41.82	86.34	41.62	86.42	42.01	—	—
%p	4.89	57.44	4.92	57.65	4.79	57.46	5.22	57.67	4.94	58.16	4.91	58.36	4.70	57.97	—	—
%d	8.93	0.01	8.85	0.01	8.72	0.02	8.62	0.02	8.68	0.01	8.71	0.01	8.83	0.01	—	—
%f	0.04	0.01	0.04	0.01	0.02	0.01	0.02	0.01	0.04	0.01	0.04	0.01	0.04	0.01	—	—

	C_2H_5		CH_3		H		F		Cl		Br		SiH_3		Ph	
Occupancy	Au	C	Au	C	Au	C	Au	C	Au	C	Au	C	Au	C	Au	C
Occupancy Au–C	1.88618		1.88684		1.88708		1.89018		1.88653		1.88509		1.88469		1.88872	
%	23.91	76.09	23.82	76.18	23.60	76.40	23.53	76.47	23.58	76.42	23.60	76.40	23.80	76.20	23.89	76.11
%s	78.80	41.46	78.86	41.39	79.01	41.59	78.75	41.74	78.96	41.17	79.03	40.95	79.15	40.99	78.93	40.76
%p	4.39	58.52	4.40	58.59	4.34	58.39	4.69	58.23	4.42	58.81	4.35	59.03	4.12	58.99	4.37	59.22
%d	16.74	0.01	16.67	0.01	16.59	0.01	16.52	0.01	16.55	0.01	16.55	0.01	16.66	0.01	16.63	0.01
%f	0.07	0.01	0.07	0.01	0.07	0.01	0.04	0.01	0.07	0.01	0.07	0.01	0.07	0.01	0.07	0.01

Chemical Valence (NOCV)[65] was performed using the ADF 2013 program package. The calculations employed the BP86-D3 functional and the TZ2P basis set for the relevant complexes. Four key parameters were analyzed in the EDA calculations. The first, ΔE_{Pauli}, accounts for repulsive interactions between fragments, stemming from the principle that two electrons with identical spins cannot occupy the same spatial region, typically resulting in positive values. The second parameter, ΔE_{elstat}, represents the electrostatic interaction energy between fragments, derived from the frozen electron density distribution of the fragments in the molecular structure. The third parameter, ΔE_{orb}, captures covalent attractions in the M–L bonds. The fourth parameter, ΔE_{dis}, reflects the energy change due to dispersion interactions, which arise from attractive forces between transient dipoles formed in molecules. These calculations aimed to investigate the nature of the $C_{(\text{tetrakis-NHC})} \rightarrow M_4$ bond in the complexes $[L_2(R)_8 \rightarrow M_4]^{4+}$; M = Ag(I) and Au(I); R = C_2H_5, CH_3, H, F, Cl, Br, SiH_3 and Ph. The total interaction energy was computed using eqn (4).

Table 6 Most important donor–acceptor interactions analysis (kcal mol^{-1}) of $[L_2(R)_8 \rightarrow M_4]^{4+}$ complexes; M = Ag(I) and Au(I); R = C_2H_5, CH_3, H, F, Cl, Br, SiH_3 and Ph

		R							
Donor–acceptor	Type	C_2H_5	CH_3	H	F	Cl	Br	SiH_3	Ph
$[L_2(R)_8 \rightarrow Ag_4]^{4+}$									
Ag_1–$C_{(NHC)1}$ → Ag_2	σ → LP*	66.11	60.61	51.35	47.22	57.23	60.01	60.99	3.87
Ag_2–$C_{(NHC)2}$ → Ag_1	σ* → LP*	—	—	—	—	40.50	50.51	—	—
Ag_1 → $C_{(NHC)1'}$–Ag_1	LP → σ*	56.22	39.79	21.14	18.34	36.40	38.12	42.63	—
Ag_2 → $C_{(NHC)2}$–Ag_2	LP* → σ*	26.25	10.39	30.08	—	—	13.16	19.99	—
$C_{(NHC)1}$ → $C_{(NHC)1'}$–Ag_1	LP → σ*	61.47	66.65	55.16	55.88	64.08	63.31	61.94	—
$C_{(NHC)1}$ → Ag_1	LP → LP*	16.41	18.37	16.53	16.99	17.16	16.81	16.81	
Ag_1 → $C_{(NHC)1}$	LP → LP*	—	—	—	6.96	—	4.62	4.58	6.90
$[L_2(R)_8 \rightarrow Au_4]^{4+}$									
Au_1 → Au_2–$C_{(NHC)2}$	σ → LP*	42.71	38.52	39.78	36.67	38.29	38.64	39.46	37.56
Au_1–$C_{(NHC)1}$ → Au_2	σ* → LP*	30.46	25.26	34.6	28.98	30.78	29.64	34.70	29.43
Au_2–$C_{(NHC)2}$ → Au_1	σ* → LP*	38.71	32.21	29.24	24.69	23.92	22.20	24.75	21.5
$C_{(NHC)1}$ → Au_1	LP → LP*	22.45	23.46	22.38	23.47	23	22.36	20.98	23.51
$C_{(NHC)1}$ → Au_2–$C_{(NHC)2}$	LP → σ*	122.65	124.22	121.26	119.34	122.00	121.44	121.11	124.13
$C_{(NHC)}$ → Au	σ* → LP*	20.18	—	29.24	24.69	23.92	22.2	34.70	21.5
Au_1–$C_{(NHC)1}$ → $C_{(NHC)1'}$	σ → LP	15.26	14.9	—	—	—	—	—	—
Au_2 → $C_{(NHC)2}$–$Au_{2'}$	LP* → σ*	31.52	26.13	24.48	22.44	24.90	—	—	10.18

Table 7 Energy decomposition analysis (EDA), (kcal mol^{-1}) of $[L_2(R)_8 \rightarrow M_4]^{4+}$ complexes; $[L_2(R)_8 \rightarrow M_4]^{4+}$ complexes; M = Ag(I), and Au(I); R = C_2H_5, CH_3, H, F, Cl, Br, SiH_3 and Ph

M	R	Fragments	ΔE_{Pauli}	ΔE_{elast}	ΔE_{orb}	ΔE_{dis}	ΔE_{int}
Ag	C_2H_5	A–BA′	544.41	−551.66(59%)	−338.88(37%)	−37.41(4%)	−383.55
Ag	C_2H_5	A–B	459.66	−595.10(56%)	−445.81(42%)	−27.01(2%)	−608.25
Ag	CH_3	A–BA′	508.01	−532.45(60%)	−323.71(36%)	−31.18(4%)	−379.33
Ag	CH_3	A–B	432.72	−576.47(56%)	−426.50(41%)	−26.02(3%)	−596.27
Ag	H	A–BA′	465.75	−500.98(60%)	−310.42(37%)	−29.35(3%)	−375.01
Ag	H	A–B	417.65	−542.17(56%)	−398.23(41%)	−25.06(3%)	−547.80
Ag	F	A–BA′	447.58	−453.84(58%)	−300.70(38%)	−29.40(4%)	−336.36
Ag	F	A–B	398.98	−479.40(53%)	−400.56(44%)	−25.08(3%)	−506.06
Ag	Cl	A–BA′	469.82	−455.92(57%)	−315.99(39%)	−31.41(4%)	−333.51
Ag	Cl	A–B	402.69	−475.38(51%)	−435.74(46%)	−26.20(3%)	−534.35
Ag	Br	A–BA′	490.81	−455.13(55%)	−340.77(41%)	−32.41(4%)	−337.49
Ag	Br	A–B	404.15	−464.79(48%)	−465.84(49%)	−26.70(3%)	−553.17
Ag	SiH_3	A–BA′	492.20	−497.45(58%)	−330.60(38%)	−34.01(4%)	−369.86
Ag	SiH_3	A–B	427.28	−520.04(52%)	−451.82(45%)	−27.14(3%)	−571.71
Ag	Ph	A–BA′	473.41	−491.37(59%)	−308.78(37%)	−31.78(4%)	−358.52
Ag	Ph	A–B	417.82	−524.70(52%)	−447.58(45%)	−26.15(3%)	−580.81
Au	C_2H_5	A–BA′	802.94	−760.44(61%)	−445.92(36%)	−43.26(3%)	−446.68
Au	C_2H_5	A–B	696.01	−791.68(55%)	−620.66(43%)	−32.28(2%)	−748.61
Au	CH_3	A–BA′	781.58	−751.90(61%)	−444.27(36%)	−36.58(3%)	−451.18
Au	CH_3	A–B	686.56	−785.91(56%)	−601.41(42%)	−30.55(2%)	−731.31
Au	H	A–BA′	747.33	−722.57(61%)	−433.71(36%)	−34.39(3%)	−443.35
Au	H	A–B	673.69	−752.01(56%)	−558.70(42%)	−29.32(2%)	−666.33
Au	F	A–BA′	743.55	−666.17(57%)	−458.10(40%)	−34.63(3%)	−415.33
Au	F	A–B	650.11	−681.60(54%)	−564.44(44%)	−29.61(2%)	−625.55
Au	Cl	A–BA′	763.35	−696.10(59%)	−445.02(38%)	−37.86(3%)	−415.63
Au	Cl	A–B	656.01	−711.30(53%)	−592.59(44%)	−31.38(3%)	−679.25
Au	Br	A–BA′	750.00	−662.82(58%)	−453.70(39%)	−38.28(3%)	−404.80
Au	Br	A–B	644.79	−663.75(50%)	−621.04(47%)	−31.75(3%)	−671.75
Au	SiH_3	A–BA′	762.21	−709.70(59%)	−452.68(38%)	−39.98(3%)	−441.15
Au	SiH_3	A–B	675.27	−725.17(52%)	−631.91(46%)	−32.18(2%)	−713.99
Au	Ph	A–BA′	793.11	−712.52(58%)	−474.74(39%)	−37.35(3%)	−431.50
Au	Ph	A–B	668.90	−732.94(53%)	−609.70(44%)	−30.89(3%)	−704.63

$$\Delta E_{int} = \Delta E_{elstat} + \Delta E_{orb} + \Delta E_{Pauli} + \Delta E_{disp} \quad (4)$$

As described earlier, the complexes $[L_2(R)_8 \rightarrow M_4]^{4+}$ (where M = Ag(I) or Au(I); R = C_2H_5, CH_3, H, F, Cl, Br, SiH_3 and Ph) were partitioned into three molecular fragments: A, A′, and B. To investigate the nature of interfragment interactions, energy decomposition analysis (EDA) was performed on the A–B and A–BA′ fragment pairs using the ADF 2013 software suite at the BP86-D3/TZ2P//PBE-D3/def2-SVP level of theory. Input files were constructed based on the optimized geometries of the complexes, and the EDA results are summarized in Table 7. The calculated interaction energies reveal two general trends. First, for a given metal center (Ag or Au), an increase in the electron-donating character of the substituent R leads to higher interaction energies. For instance, in the Au(I) series, the interaction energies for the $[L_2(Ph)_8 \rightarrow Au_4]^{4+}$ complex are −704.63 kcal mol^{-1} and −431.50 kcal mol^{-1} for the A–B and A–BA′ fragments, respectively, whereas for $[L_2(F)_8 \rightarrow Au_4]^{4+}$, the corresponding values are lower at −625.55 kcal mol^{-1} and −415.33 kcal mol^{-1}. Second, for a fixed R substituent, the complexes with Au(I) exhibit stronger interactions than their Ag(I) counterparts. For instance, the $[L_2(CH_3)_8 \rightarrow Au_4]^{4+}$ complex exhibits interaction energies of −731.31 kcal mol^{-1} for the A–B fragment and −451.18 kcal mol^{-1} for the A–BA′ fragment. In comparison, the corresponding Ag(I) complex shows values of −596.27 kcal mol^{-1} and −379.33 kcal mol^{-1}, respectively. Among all the complexes examined, The strongest A–B and A–BA′ interactions were observed in $[L_2(C_2H_5)_8 \rightarrow Au_4]^{4+}$ (−748.61 kcal mol^{-1}) and $[L_2(CH_3)_8 \rightarrow Au_4]^{4+}$ (−451.18 kcal mol^{-1}), respectively, whereas the weakest were found in $[L_2(F)_8 \rightarrow Ag_4]^{4+}$ (−506.06 kcal mol^{-1}) and $[L_2(Cl)_8 \rightarrow Ag_4]^{4+}$ (−333.51 kcal mol^{-1}), respectively. Notably, these computational results are consistent with those interaction energies calculated at the PBE-D3/def2-TZVP//PBE-D3/def2-SVP level of theory.

The EDA results reveal that electrostatic interactions (ΔE_{elstat}) are the dominant contributors to the total interaction energy in all complexes investigated here. For A–B fragments, ΔE_{elstat} accounted for (48–56%) of the total interaction energy in Ag(I) complexes and (50–56%) in Au(I) complexes. Similarly, for A–BA′ fragments, the corresponding ranges were (55–60%) for Ag(I) and (57–61%) for Au(I). In contrast, orbital interactions (ΔE_{orb}) contributed (41–49%) for A–B and (36–41%) for A–BA′ in Ag(I) complexes, while in Au(I) complexes, these values ranged from (42–47%) and (36–40%), respectively. The highest ΔE_{elstat} percentage for the A–B fragment was observed in $[L_2(R)_8 \rightarrow Ag_4]^{4+}$ (R = C_2H_5, CH_3, and H) and $[L_2(R)_8 \rightarrow Au_4]^{4+}$ (R = CH_3 and H) at 56%, whereas for the A–BA′ fragment it was observed

Table 8 Calculated values of $\Delta\Delta E_{Pauli}$, $\Delta\Delta E_{elstat}$, $\Delta\Delta E_{orb}$, $\Delta\Delta E_{dis}$ and $\Delta\Delta E_{int}$ in A–B and A–BA′ bonds, (kcal mol^{-1}) of $[L_2(R)_8 \rightarrow M_4]^{4+}$ complexes; $[L_2(R)_8 \rightarrow M_4]^{4+}$ complexes; M = Ag(I), and Au(I); R = C_2H_5, CH_3, H, F, Cl, Br, SiH_3 and Ph

M	R	$\Delta\Delta E_{Pauli}$	$\Delta\Delta E_{elast}$	$\Delta\Delta E_{orb}$	$\Delta\Delta E_{dis}$	$\Delta\Delta E_{int}$	IE_{coop}
Ag	C_2H_5	84.75	43.44	106.93	−10.4	224.72	246.74
Ag	CH_3	75.29	44.02	102.79	−5.16	216.94	233.78
Ag	H	48.1	41.19	87.81	−4.29	172.81	185.73
Ag	F	48.6	25.56	99.86	−4.32	169.7	176.01
Ag	Cl	67.13	19.46	119.75	−5.21	201.13	207.98
Ag	Br	86.66	9.66	125.07	−5.71	215.68	225.73
Ag	SiH_3	64.92	22.59	121.22	−6.87	201.86	225.32
Ag	Ph	55.59	33.33	138.8	−5.63	222.09	233.13
Au	C_2H_5	106.93	31.24	174.74	−10.98	301.93	309.14
Au	CH_3	95.02	34.01	157.14	−6.03	280.14	295.08
Au	H	73.64	29.44	124.99	−5.07	223.00	236.61
Au	F	93.44	15.43	106.34	−5.02	210.19	222.56
Au	Cl	107.34	15.2	147.57	−6.48	263.63	285.22
Au	Br	105.21	0.93	167.34	−6.53	266.95	279.30
Au	SiH_3	86.94	15.47	179.23	−7.8	273.84	283.52
Au	Ph	124.21	20.42	134.96	−6.46	273.13	287.65

in $[L_2(R)_8 \rightarrow Au_4]^{4+}$ (R = C_2H_5, CH_3, and H) at 61%. Conversely, the lowest ΔE_{elstat} values were recorded for $[L_2(Br)_8 \rightarrow Ag_4]^{4+}$ (48%) in A–B and $[L_2(Br)_8 \rightarrow Au_4]^{4+}$ (50%) in A–BA′ fragments. For ΔE_{orb}, the highest contribution was observed in $[L_2(Br)_8 \rightarrow Ag_4]^{4+}$ (49%) for the A–B fragment and in $[L_2(Br)_8 \rightarrow Ag_4]^{4+}$ (41%) for the A–BA′ fragment. The lowest ΔE_{orb} values were observed for the A–B fragment in $[L_2(CH_3)_8 \rightarrow Ag_4]^{4+}$ and $[L_2(H)_8 \rightarrow Ag_4]^{4+}$ (41%) and for the A–BA′ fragment in $[L_2(CH_3)_8 \rightarrow Ag_4]^{4+}$ and $[L_2(R)_8 \rightarrow Au_4]^{4+}$ (R = C_2H_5, CH_3, and H) (36%). Overall, the EDA outcomes indicate that the bonding in these coinage metal complexes is predominantly electrostatic in nature, with significant contributions from covalent (orbital) interactions depending on both the metal center and the nature of the substituents. One of us and his coworker, based on eqn (4), considered the difference in interaction energy between two bonds to arise from variations in the four components of this equation, and, for a clearer comparison, eqn (5) was rewritten as follows.[61] Moreover, based on eqn (S3), when comparing the A–B and A–BC bonds (or B–C and AB–C bonds), the value of $\Delta\Delta E_{int}$ represents the cooperative interaction energy (ΔE_{coop}). Therefore, analyzing and comparing the contributions of these components can clarify the origin of positive or negative cooperativity.

$$\Delta\Delta E_{int} = \Delta\Delta E_{Pauli} + \Delta\Delta E_{elstat} + \Delta\Delta E_{orb} + \Delta\Delta E_{dis} \quad (5)$$

The calculated values of $\Delta\Delta E_{Pauli}$, $\Delta\Delta E_{elstat}$, $\Delta\Delta E_{orb}$, $\Delta\Delta E_{dis}$ and $\Delta\Delta E_{int}$ for A–B and A–BA′ bonds are presented and summarized in Table 8. The results reveal that the primary contributor to the positive cooperativity in these complexes is the ΔE_{orb} term. This is followed, in order of significance, by Pauli repulsion and the ΔE_{elstat} component. In contrast, the ΔE_{disp} term contributes negatively; however, its relatively minor contribution prevents it from exerting a significant influence on the overall outcome. Thus, the origin of the anti-cooperativity of the bonds in the present complexes is the unfavorable changes in Pauli repulsion, electrostatic attractions, and especially orbital attractions upon the impact of the metal–ligand bonds on each other.

EDA-NOCV analysis

The Natural Orbitals for Chemical Valence (NOCV) method is a valuable computational tool for probing chemical bonding in molecular systems. Energy Decomposition Analysis (EDA) partitions the total interaction energy (ΔE_{int}) into its fundamental components, while the NOCV method provides a detailed breakdown of the orbital interaction term (ΔE_{orb}). When combined, the EDA-NOCV framework allows for the decomposition of the total deformation density ($\Delta\rho$) associated with bond formation into individual chemically meaningful contributions. This integrated analysis facilitates a more quantitative understanding of the nature of metal–ligand (M–L) bonding. In this study, NOCV calculations were performed for the fragment pairs A–B and A–BA′. The results for the $[L_2(Ph)_8 \rightarrow Au_4]^{4+}$ complex are illustrated in Fig. 8. The electron density distributions between the M_4^+ fragment and the $L_2(R)_8$ ligand framework, along with the associated orbital energy contributions for the remaining complexes $[L_2(R)_8 \rightarrow M_4]^{4+}$ (where M = Ag(I), Au(I); R = C_2H_5, CH_3, H, F, Cl, Br, SiH_3, and Ph), are summarized in Fig. S1 and S2. The NOCV analysis revealed that the primary deformation densities ($\Delta\rho_1$, $\Delta\rho_2$, and $\Delta\rho_3$) contributing to the $C_{(tetrakis\text{-}NHC)} \rightarrow M_4$ interaction in both A–B and A–BA′ fragments are predominantly of σ-type character. These interactions originate from the donation of the non-bonding electron pair on the carbon atom ($C_{(tetrakis\text{-}NHC)}$) into the vacant d-orbitals of the metal center. This σ-type donation constitutes the dominant bonding component in these coinage metal–NHC complexes. In $\Delta\rho_1$, the charge density is transferred from the lone pairs of the carbene carbon atoms—two located at the upper part of the complex and two bridging carbene carbons that link the ligands—toward a metal atom. In $\Delta\rho_2$ and $\Delta\rho_3$, the charge density is transferred from the lone pairs of the four bridging carbene carbon atoms to three metal atoms. Deformation density analysis (NOCV) indicates that $\Delta\rho_1$, $\Delta\rho_2$, and $\Delta\rho_3$ increase from Ag(I) to Au(I), with the sum $\Delta\rho_1 + \Delta\rho_2 + \Delta\rho_3$ generally larger for clusters with electron-donating substituents, reflecting stronger overall ligand-to-metal charge transfer. It should be noted that the metal centers investigated in this study, Ag(I) and Au(I), possess a closed-shell d^{10} electronic configuration, which strongly limits π-back-donation. Consequently, the $C_{(tetrakis\text{-}NHC)} \rightarrow M_4$ interactions in these complexes are inherently dominated by σ-donation from the carbene carbon lone pair to the vacant metal orbitals. Within this electronic framework, the NOCV analysis is primarily employed to visualize the dominant charge-flow channels associated with σ-donation. Although the deformation density plots are presented qualitatively, they are fully consistent with the quantitative Energy Decomposition Analysis (EDA) results, which explicitly show that the orbital interaction term (ΔE_{orb}) is a major contributor to the overall metal–ligand bonding. In particular, the stronger Au–C interactions relative to Ag–C are already

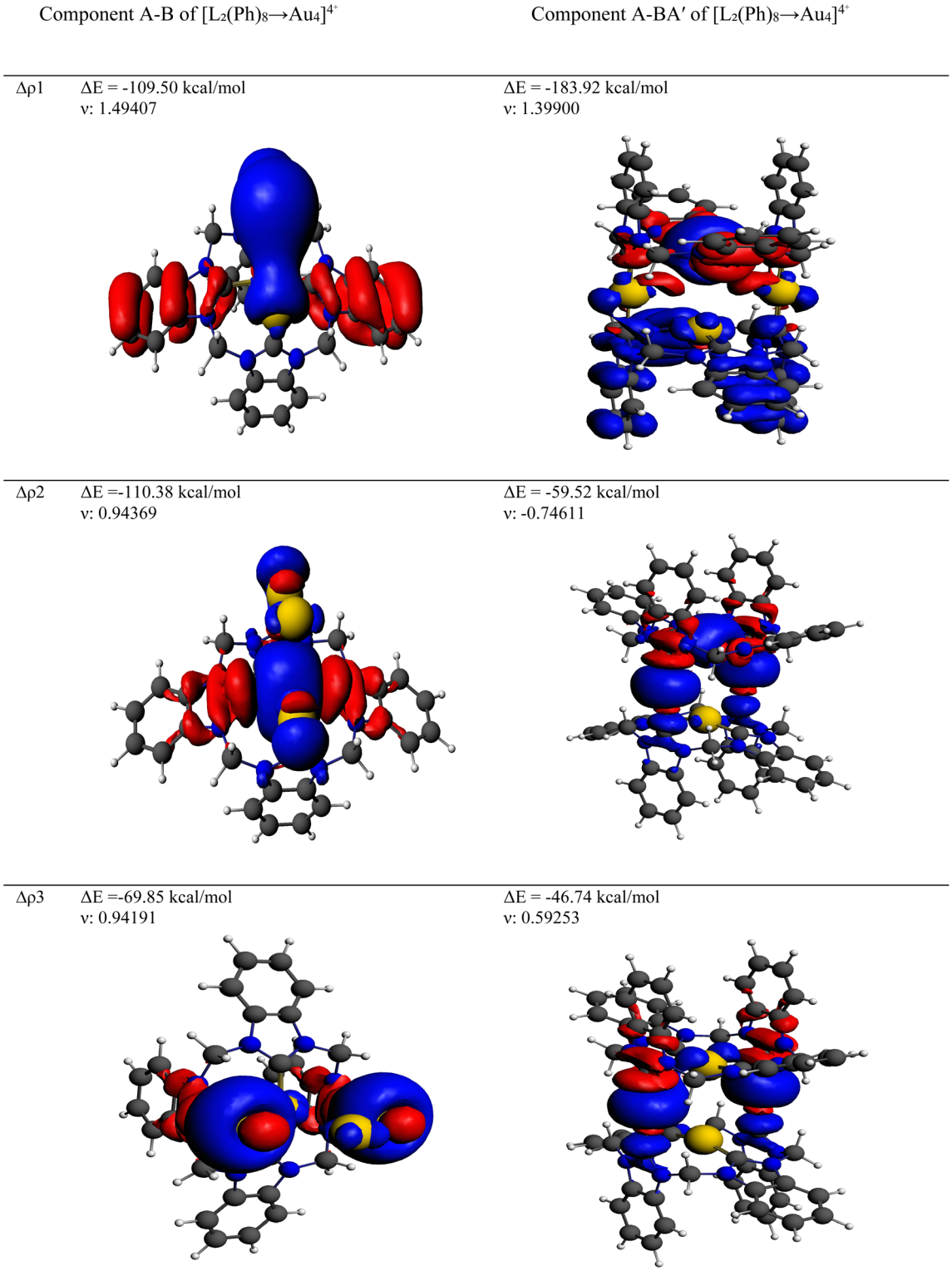

Fig. 8 Contour plots of NOCV deformation densities $\Delta\rho$ and associated energies $\Delta E(\rho)$ of the $[L_2(Ph)_8 \rightarrow Au_4]^{4+}$ complex for A–B and A–BA′ components, computed at the BP86-D3/TZ2P level of theory. The corresponding deformation electron densities were depicted by the direction of charge transitioning from red to blue. The eigenvalues (ν) give the size of the charge migration.

quantitatively captured by the larger ΔE_{orb} values obtained from EDA.

Therefore, the combined EDA-NOCV approach provides both qualitative and quantitative insight into the bonding nature, with EDA delivering the energetic metrics required for comparison, and NOCV serving as a complementary tool to elucidate the physical origin of the dominant σ-donation in Ag–C and Au–C bonds.

Conclusion

A theoretical investigation on the nature and cooperativity of metal–ligand bonds in series tetranuclear Ag(I) and Au(I) complexes, $[L_2(R)_8 \rightarrow M_4]^{4+}$ (M = Ag(I) and Au(I); R = C_2H_5, CH_3, H, F, Cl, Br, Ph, and SiH_3), was performed at the PBE-D3/def2-SVP//PBE-D3/def2-TZVP level of theory. Bonding was analyzed through NBO, EDA, and EDA-NOCV methods. Interaction energies between the A–B and A–BA′ fragments revealed consistently higher values for Au(I) complexes compared to Ag(I) analogues. Cooperativity values were positive for all clusters, indicating anti-cooperative behavior, with the trend Ag(I) < Au(I) mirroring that of the interaction energies. The effect of substituents was also elucidated: electron-donating groups increased the interaction energies and slightly enhanced the anti-cooperative behavior compared to electron-withdrawing groups. NOCV analysis of the primary deformation densities ($\Delta\rho_1$, $\Delta\rho_2$, and $\Delta\rho_3$) showed an increasing trend from Ag(I) to Au(I), with the sum $\Delta\rho_1 + \Delta\rho_2 + \Delta\rho_3$ generally larger for electron-donating substituents, consistent with stronger overall ligand-to-metal σ-donation. In all cases, the electrostatic component remained the dominant contributor to the total interaction energy, highlighting the electrostatic nature of the metal–ligand interactions. These results provide a comprehensive understanding of bonding, substituent effects, and cooperativity in tetranuclear group-11 clusters, offering a solid foundation for future studies on their potential biological relevance.

Conflicts of interest

The authors declare no competing financial interest.

Data availability

The data supporting this article have been included as part of the supplementary information (SI). Supplementary information: includes the optimized Cartesian (*XYZ*) coordinates of all investigated structures, fully optimized geometries, and intrinsic reaction coordinate (IRC) plots. It also provides detailed derivations, mathematical formulations, and representative sample calculations related to cooperativity analysis. In addition, extended data on M–C bond lengths and the corresponding NOCV energy decomposition schemes are presented to support the discussions in the main manuscript. See DOI: https://doi.org/10.1039/d5na00870k.

References

1 D. Bourissou, O. Guerret, F. P. Gabbai and G. Bertrand, *Chem. Rev.*, 2000, **100**, 39–92.
2 R. H. Crabtree, *J. Organomet. Chem.*, 2005, **690**, 5451–5457.
3 S. P. Nolan, *N-Heterocyclic Carbenes in Synthesis*, 2006.
4 F. Glorius, in *N-Heterocyclic Carbenes in Transition Metal Catalysis*, 2007, ch. 59, pp. 1–20, DOI: 10.1007/978-3-540-36930-1.
5 F. E. Hahn and M. C. Jahnke, *Angew Chem. Int. Ed. Engl.*, 2008, **47**, 3122–3172.
6 A. A. Danopoulos, T. Simler and P. Braunstein, *Chem. Rev.*, 2019, **119**, 3730–3961.
7 S. Diez-Gonzalez, N. Marion and S. P. Nolan, *Chem. Rev.*, 2009, **109**, 3612–3676.
8 P. de Frémont, N. Marion and S. P. Nolan, *Coord. Chem. Rev.*, 2009, **253**, 862–892.
9 T. Scattolin and S. P. Nolan, *Trends Chem.*, 2020, **2**, 721–736.
10 E. van Vuuren, F. P. Malan and M. Landman, *Coord. Chem. Rev.*, 2021, **430**, 5203–5215.
11 W. A. Herrmann, *Angew Chem. Int. Ed. Engl.*, 2002, **41**, 1290–1309.
12 M. Poyatos, J. A. Mata and E. Peris, *Chem. Rev.*, 2009, **109**, 3677–3707.
13 J. C. Lin, R. T. Huang, C. S. Lee, A. Bhattacharyya, W. S. Hwang and I. J. Lin, *Chem. Rev.*, 2009, **109**, 3561–3598.
14 L. Oehninger, R. Rubbiani and I. Ott, *Dalton Trans.*, 2013, **42**, 3269–3284.
15 F. Cisnetti and A. Gautier, *Angew Chem. Int. Ed. Engl.*, 2013, **52**, 11976–11978.
16 S. P. Nolan, *Acc. Chem. Res.*, 2011, **44**, 91–100.
17 F. Lazreg, F. Nahra and C. S. J. Cazin, *Coord. Chem. Rev.*, 2015, **293–294**, 48–79.
18 A. Kascatan-Nebioglu, A. Melaiye, K. Hindi, S. Durmus, M. J. Panzner, L. A. Hogue, R. J. Mallett, C. E. Hovis, M. Coughenour, S. D. Crosby, A. Milsted, D. L. Ely, C. A. Tessier, C. L. Cannon and W. J. Youngs, *J. Med. Chem.*, 2006, **49**, 6811–6818.
19 K. M. Hindi, M. J. Panzner, C. A. Tessier, C. L. Cannon and W. J. Youngs, *Chem. Rev.*, 2009, **109**, 3859–3884.
20 L. Mercs and M. Albrecht, *Chem. Soc. Rev.*, 2010, **39**, 1903–1912.
21 S. Ray, R. Mohan, J. K. Singh, M. K. Samantaray, M. M. Shaikh, D. Panda and P. Ghosh, *J. Am. Chem. Soc.*, 2007, **129**, 15042–15053.
22 M. L. Teyssot, A. S. Jarrousse, M. Manin, A. Chevry, S. Roche, F. Norre, C. Beaudoin, L. Morel, D. Boyer, R. Mahiou and A. Gautier, *Dalton Trans.*, 2009, 6894–6902, DOI: 10.1039/b906308k.
23 Ö. D. Ulu, A. Kuruçay, B. Ateş and İ. Özdemir, *Chem. Pap.*, 2022, **77**, 423–435.
24 P. O. Asekunowo, R. A. Haque and M. R. Razali, *Rev. Inorg. Chem.*, 2017, **37**, 29–50.
25 W. Liu and R. Gust, *Chem. Soc. Rev.*, 2013, **42**, 755–773.
26 H. G. Raubenheimer and S. Cronje, *Chem. Soc. Rev.*, 2008, **37**, 1998–2011.

27 J. L. Hickey, R. A. Ruhayel, P. J. Barnard, M. V. Baker, S. J. Berners-Price and A. Filipovska, *J. Am. Chem. Soc.*, 2008, **130**, 12570–12571.
28 M. V. Baker, P. J. Barnard, S. J. Berners-Price, S. K. Brayshaw, J. L. Hickey, B. W. Skelton and A. H. White, *J. Organomet. Chem.*, 2005, **690**, 5625–5635.
29 P. J. Barnard, M. V. Baker, S. J. Berners-Price and D. A. Day, *J. Inorg. Biochem.*, 2004, **98**, 1642–1647.
30 M. M. Jellicoe, S. J. Nichols, B. A. Callus, M. V. Baker, P. J. Barnard, S. J. Berners-Price, J. Whelan, G. C. Yeoh and A. Filipovska, *Carcinogenesis*, 2008, **29**, 1124–1133.
31 D. Krishnamurthy, M. R. Karver, E. Fiorillo, V. Orru, S. M. Stanford, N. Bottini and A. M. Barrios, *J. Med. Chem.*, 2008, **51**, 4790–4795.
32 J. Rieb, B. Dominelli, D. Mayer, C. Jandl, J. Drechsel, W. Heydenreuter, S. A. Sieber and F. E. Kuhn, *Dalton Trans.*, 2017, **46**, 2722–2735.
33 P. J. Barnard, L. E. Wedlock, M. V. Baker, S. J. Berners-Price, D. A. Joyce, B. W. Skelton and J. H. Steer, *Angew Chem. Int. Ed. Engl.*, 2006, **45**, 5966–5970.
34 G. Roymahapatra, S. M. Mandal, W. F. Porto, T. Samanta, S. Giri, J. Dinda, O. L. Franco and P. K. Chattaraj, *Curr. Med. Chem.*, 2012, **19**, 4184–4193.
35 P. K. Behera, L. Maity, S. Roy, A. Das, P. Sahu, H. K. Kisan, A. Changotra, A. A. Isab, M. B. Fettouhi, A. Bairagi, N. Chatterjee and J. Dinda, *New J. Chem.*, 2023, **47**, 18835–18848.
36 C. H. G. Jakob, A. W. Muñoz, J. F. Schlagintweit, V. Weiß, R. M. Reich, S. A. Sieber, J. D. G. Correia and F. E. Kühn, *J. Organomet. Chem.*, 2021, 932.
37 M. Rezaeivala, M. Ahmadi, B. Captain, M. Bayat, M. Saeidirad, S. Şahin-Bölükbaşı, B. Yıldız and R. W. Gable, *Inorg. Chim. Acta*, 2020, **513**, 119935.
38 B. Naderizadeh and M. Bayat, *Mendeleev Commun.*, 2021, **31**, 179–181.
39 B. Naderizadeh and M. Bayat, *ACS Omega*, 2020, **5**, 26999–27015.
40 B. Naderizadeh, M. Bayat, M. Ranjbaran and S. Salehzadeh, *J. Mol. Liq.*, 2021, **341**, 117310.
41 T. Simler, P. Braunstein and A. A. Danopoulos, *Dalton Trans.*, 2016, **45**, 5122–5139.
42 K. Naeimi, M. Bayat and E. Alavi Pour, *RSC Adv.*, 2025, **15**, 6742–6752.
43 E. B. Bauer, M. A. Bernd, M. Schutz, J. Oberkofler, A. Pothig, R. M. Reich and F. E. Kuhn, *Dalton Trans.*, 2019, **48**, 16615–16625.
44 J. P. Perdew, K. Burke and M. Ernzerhof, *Phys. Rev. Lett.*, 1996, **77**, 3865–3868.
45 S. Grimme, S. Ehrlich and L. Goerigk, *J. Comput. Chem.*, 2011, **32**, 1456–1465.
46 M. Frisch *et al.*, *Gaussian 09, Revision D. 01*, Gaussian, Inc., Wallingford CT, 2009, https://www.gaussian.com.
47 G. te Velde, F. M. Bickelhaupt, E. J. Baerends, C. Fonseca Guerra, S. J. A. van Gisbergen, J. G. Snijders and T. Ziegler, *J. Comput. Chem.*, 2001, **22**, 931–967.
48 S. Salehzadeh and F. Maleki, *J. Comput. Chem.*, 2016, **37**, 2799–2807.
49 S. S. Movafagh and S. Salehzadeh, *Phys. Chem. Chem. Phys.*, 2024, **26**, 15005–15017.
50 C. A. Hunter and H. L. Anderson, *Angew Chem. Int. Ed. Engl.*, 2009, **48**, 7488–7499.
51 G. Ercolani and L. Schiaffino, *Angew Chem. Int. Ed. Engl.*, 2011, **50**, 1762–1768.
52 G. Ercolani and L. Schiaffino, in *Bioinspiration and Biomimicry in Chemistry*, 2012, ch. 3, pp. 47–69, DOI: 10.1002/9781118310083.
53 D. Hankins, J. W. Moskowitz and F. H. Stillinger, *Chem. Phys. Lett.*, 1970, **4**, 527–530.
54 C. Estarellas, A. Frontera, D. Quinonero and P. M. Deya, *Chemphyschem*, 2011, **12**, 2742–2750.
55 M. Solimannejad and M. Malekani, *Comput. Theor. Chem.*, 2012, **998**, 34–38.
56 M. Solimannejad, Z. Rezaei and M. D. Esrafili, *J. Mol. Model.*, 2013, **19**, 5031–5035.
57 M. D. Esrafili, P. Esmailpour, F. Mohammadian-Sabet and M. Solimannejad, *Chem. Phys. Lett.*, 2013, **588**, 47–50.
58 X. Guo, Y.-W. Liu, Q.-Z. Li, W.-Z. Li and J.-B. Cheng, *Chem. Phys. Lett.*, 2015, **620**, 7–12.
59 M. D. Esrafili, P. Fatehi and M. Solimannejad, *Comput. Theor. Chem.*, 2014, **1034**, 1–6.
60 A. Soufi and S. Salehzadeh, *J. Comput. Chem.*, 2025, **46**, e70022.
61 S. S. Movafagh, Y. Gholiee and S. Salehzadeh, *New J. Chem.*, 2024, **48**, 15045–15052.
62 S. Salehzadeh and S. Sanei Movafagh, *Comments Inorg. Chem.*, 2025, 1–29, DOI: 10.1080/02603594.2025.2492221.
63 F. Weinhold, C. R. Landis and E. D. Glendening, *Int. Rev. Phys. Chem.*, 2016, **35**, 399–440.
64 M. Bayat, A. Sedghi, L. Ebrahimkhani and S. J. Sabounchei, *Dalton Trans.*, 2016, **46**, 207–220.
65 A. Sedghi, M. Bayat, S. J. Sabounchei and M. Khodabandehloo, *Polyhedron*, 2019, **157**, 208–218.
66 M. P. Mitoraj, A. Michalak and T. Ziegler, *J. Chem. Theory Comput.*, 2009, **5**, 962–975.